

## Theoretical and Experimental Research on Spatial Performances of the Long-slit Streak Tube

Liping Tian<sup>1,2</sup>, Lingbin Shen<sup>1</sup>, Yanhua Xue<sup>2</sup>, Lin Chen<sup>1</sup>, Lili Li<sup>2</sup>, Ping Chen<sup>2</sup>, Jinshou Tian<sup>2</sup>, Wei Zhao<sup>2</sup>.

<sup>1</sup>*School of network and communication engineering, Jinling Institute of Technology, Hongjing Road, No.99, Nanjing 211169, China, LB\_shen@jit.edu.cn (L. Shen)*

<sup>2</sup>*Key Laboratory of Transient Optics and Photonics, Key Laboratory of Ultra-fast Photoelectric Diagnostics Technology, Xi'an Institute of Optics and Precision Mechanics, Chinese Academy of Sciences, Xixi Road, No.17, Xi'an, 710119, China, xueyanhua@opt.ac.cn*

The streak tubes are widely used in National Ignition Facility (NIF), Inertial Confinement Fusion (ICF), and streak tube imaging lidar (STIL) as radiation or imaging detectors. The spatial resolution and effective photocathode area of the streak tube are strongly dependent on its operating and geometry parameters (electron optical structure and applied voltage). Studies about this dependence do not cover the full range of the parameters. In this paper, 3-D models are developed in Computer Simulation Technology Particle Studio (CST-PS) to comprehensively calculate the spatial resolution for various parameters. Monte Carlo Sampling method (M-C method) and spatial modulation transfer function method (SMTF) are employed in our simulation. Simulated results of the optimized spatial resolution are validated by the experimental data. Finally, the radii of the photocathode ( $R_c$ ) and phosphor screen ( $R_s$ ) are optimized. Geometry parameters of  $R_c=60$  mm and  $R_s=80$  mm are proposed to optimize the streak tube performances. Simulation and experimental results show that the spatial resolution and effective photocathode area of this streak tube are expected to reach 16 lp/mm and 30 mm-length while the voltage between cathode and grid ( $U_{cg}$ ) is 150 V.

Keywords: Ultrafast detector, Streak tube, Imaging, Spatial resolution, Temporal resolution.

### 1. INTRODUCTION

With advantages of ultra-high temporal resolution (ps~fs) and high spatial resolution ( $\mu\text{m}$ ), streak tubes are widely used in microscopic and ultrafast process detection, as well as in basic and cutting-edge scientific research. For example, a large-format streak tube, as a high sensitivity radiation device, provides X-ray spectral information in the ICF experiment. In the STIL experiment, a large effective photocathode area and a high spatial resolution would provide large numbers of pixels, thereby improving detection accuracy [1]-[3].

The streak tubes with high spatial resolution and large effective photocathode area are developed by several companies, including Photonis (France), Photek (the United Kingdom), and BIFO company (Russian) [4]. The working area of the slit streak tube P510 designed by Photonis is as large as 35 mm $\times$ 4 mm, but the disadvantages of it are the low spatial resolution of 10 lp/mm and large magnification of 1.3, which are not helpful for the enhancement of the image intensity [5]. The streak tube ST-Y is manufactured by Photek with a larger working area of 35 mm $\times$ 5 mm and a spatial resolution of 40 lp/mm. However, it has a low deflection sensitivity of 25 mm/KV, which is not a benefit to the

improvement of the temporal resolution [4]. PV400 streak tube designed by the Russian company has a larger photocathode working area of 35 mm $\times$ 4 mm compared with the above, but the center static resolution is only 35 lp/mm and the whole length of the streak tube is 375 mm, which is not a benefit to the miniaturization [6].

It is necessary to carry out theoretical design before manufacture and experiment [7]-[11]. For long-slit streak tube, however, studies and experiments investigating the dependence of the spatial resolution performances on operating and geometry parameters are sparse. In this paper, to fully understand the streak tube performances, various photocathode, phosphor screen geometries and applied voltages between photocathode and grid were systematically simulated by 3-D model, which was developed in a simulation software, Computer Simulation Technology Particle Studio Suite (CST-PS). Monte Carlo (M-C) sampling method and finite integral technology method (FIT) were adopted in our simulation. Based on the simulations, a set of geometry and operating parameters were proposed to design a long-slit streak tube with high spatial resolution. Finally, the streak tube was successfully manufactured according to the electro-optical design to validate the simulation results.

## 2. THEORY AND COMPUTER SIMULATION DETAILS

The traditional streak tubes, shown in Fig.1.a), often use a flat photocathode and phosphor screen, which would cause a large aberration, and thereby result in a low spatial resolution [12]. An accelerating electrode (mesh or grid) setting downstream from the photocathode is adopted to improve the temporal resolution by increasing the kinetic energy of the photoelectrons [13]. What should be noted is that the photocathode and the accelerating grid are usually placed in parallel to obtain a uniform electric field. In addition, the streak tube used in the STIL system requires a high luminance gain to detect the weak visible light [3]. Thus, a grid accelerating electrode is usually adopted to increase the transmittance of the photoelectrons. The streak tube with a compact structure has a length of only 235 mm and the outer diameter of the tube is 75 mm.

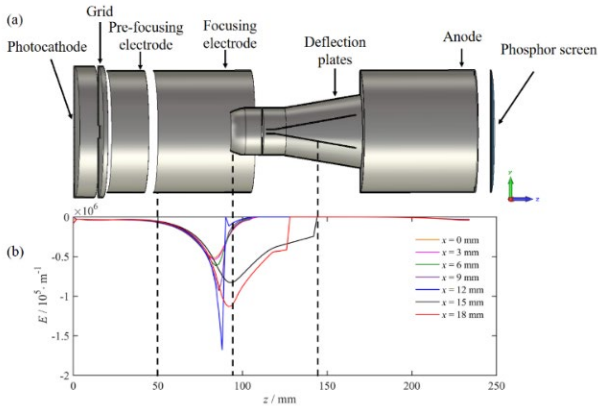


Fig.1. Schematic drawing and E-field distribution of the long-slit streak tube.

It is an obvious truism that the spatial resolution is greatly affected by the aberration of the electro-optical system of the streak tube, especially the distortion, which is related to the radii of curvature (ROCs) of the photocathode and the phosphor screen. In addition, the initial electron energy spread and accelerating voltage have great impacts on the temporal characteristics. Accordingly, in this paper, the dependence of the spatial resolution and temporal resolution on the accelerating voltage and different geometry parameters, such as ROC of the photocathode and the phosphor screen, is systematically simulated. A set of electric and geometry parameters which would contribute to achieve high spatial resolution, large effective photocathode area and good temporal resolution are proposed. The most predominant features in this new streak tube are that the spatial resolution reaches 16 lp/mm over the effective photocathode length of 30 mm and the external dimensions are about  $\Phi 150 \text{ mm} \times 249 \text{ mm}$ . This new streak tube with a photocathode radiant sensitivity of 61 mA/W and a radiant emittance gain of 16.3 at the wavelength of 400 nm was already demonstrated. All superior performances, including high photocathode radiant sensitivity, high radiant emittance gain and large effective photocathode area indicate that this streak tube can be widely used in the STIL and the ICF diagnosis system.

In this paper, CST-PS is used to build the 3-D streak tube model and calculate inner electric fields, electron trajectories based on the FIT and M-C method. Inspired by the previous research, the state of the electrons emitted from the photocathode in this paper have the following considerations.

- i . The initial energy of the electrons has  $\beta$  distribution of 0-0.6 eV.
- ii . The electrons launch elevation angle behaves according to a cosine distribution of 0~90 degrees.
- iii . The azimuths of the electrons are uniformly distributed from the range of 0~  $2\pi$ .
- iv . It should be noted that the above parameters are fully independent of each other.
- v . The voltage applied between photocathode and grid, radius of curvature of photocathode and phosphor screen are represented by  $U_{cg}$ ,  $R_c$ , and  $R_s$ , respectively. In the following simulations, only one of the parameters is varied at a time, while the others are kept constant, with initial values listed in Table 1.

Table 1. Initial values of the parameters.

$U_{cg}$	$R_c$	$R_s$
100 V	$+\infty(+\text{inf})$	$+\infty(+\text{inf})$

## 3. RESULTS

### A. The electric field distribution and the calculation of the electron trajectories.

The axial electric field distribution at different distances from the axis inside the streak tube is simulated, shown in Fig.1.b), where  $x$  represents the off-axis distance. Obviously, the photoelectrons emitted from the photocathode are always accelerated, causing the negative electric field between the photocathode and the phosphor screen. Whether on- or off-axis, the electric field increases first in the negative direction and then decreases in the axis direction, until reaching the maximum in the region from the focusing electrode to the anode hole. According to the design method, all electrons that travel near the anode hole would be focused and move close to the axis. It means that the electric field experienced is mainly over the range of  $r=0\sim 6 \text{ mm}$ . It is well explained that the axis electric field affects the operating speed of the photoelectrons, but the impact is only small. The discrete Lorentz Force law is used to calculate the electron trajectory after obtaining the electric field distribution. In this long-slit streak tube, the influence of the magnetic field on the electrons can be ignored. Just insert the electric field value presented by formulas (1) and (2) into the discrete Lorentz Force law, demonstrated by formulas (3) and (4).

$$\frac{d}{dt}(m\vec{v}) = q(\vec{E} + \vec{v} \times \vec{B}) \quad (1)$$

$$\frac{d\vec{r}}{dt} = \vec{v} \quad (2)$$

$$m^{n+1}\vec{v}^{n+1} = m^n\vec{v}^n + q\Delta t(\vec{E}^{n+1/2} + \vec{v}^{n+1/2} \times \vec{B}^{n+1/2}) \quad (3)$$

$$\vec{r}^{n+3/2} = \vec{r}^{n+1/2} + \Delta t \vec{v}^{n+1} \quad (4)$$

where  $m$  and  $\vec{v}$  are electronic mass and speed,  $\vec{E}$  and  $\vec{B}$  are electric and magnetic field distribution of the streak tube,  $\vec{r}$  is off-axis distance.

### B. Dependence of the spatial resolution and temporal resolution on the $R_c$

As shown in Fig.2., the spatial resolution distributions for  $R_c = +\text{inf}$ , 75, 85, and 95 mm essentially decrease with off-axis distance, with the spatial resolution of 11, 15, 19, and 12 lp/mm at off-axis distance of 15 mm, respectively. The spatial resolution increases with increasing  $R_c$ , until its maximum 19 lp/mm at off-axis distance of 15 mm and then decreases, which is a consequence of the reduction of the aberrations, especially reduction of distortion at the edge. Obviously, the electron beam at the off-axis of 15 mm is underfocused at  $R_c=75$  mm and overfocused at  $R_c=95$  mm, which both result in a low spatial resolution. Spatial resolution for the  $R_c=85$  mm case is significantly higher than that of the other case, especially at the edge.

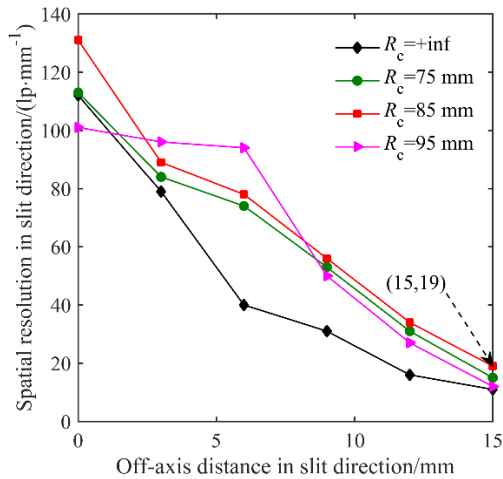


Fig.2. Spatial resolution as a function of  $R_c$  over the range of  $+\text{inf}$ , 75 mm to 95 mm by the step of 10 mm.

The temporal resolution of an electro-optical system is known as the transit time dispersion of the electrons emitted from the photocathode to the photocathode, traveling from the special point on the photocathode to the phosphor screen. The transit time dispersion is caused not only because of the variations in photoelectron initial energy, initial launch elevation angle, and azimuth, but it also depends on the space charge effect contributed by the number of the electrons and electric field. To improve the temporal resolution uniformity, curved spherical photocathode is considered to eliminate the time distortion by shortening the optical path differences between the photoelectrons emitted from the different location of the photocathode. Fig.3. shows the simulated temporal resolution distribution of the streak tube for  $R_c = +\text{inf}$ , 75 mm, 85 mm, and 95 mm. The temporal resolution deteriorates with the increasing off-axis distance. It is because

electron pulses off-axis suffer larger longitudinal time dispersion than those of the electron pulses at the center. The temporal resolution deteriorates the most while we adopt a flat ( $R_c = +\text{inf}$ ) photocathode. In addition, it is better than 50 ps, and there is almost no difference when the  $R_c = 75$  mm, 85 mm, and 95 mm.

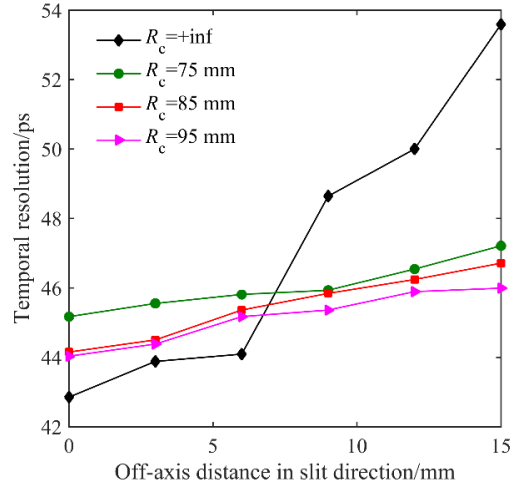


Fig.3. Temporal resolution as a function of  $R_c$  over the range of  $+\text{inf}$ , 75 mm to 95 mm by the step of 10 mm.

### C. Dependence of the spatial resolution and temporal resolution on the $R_s$

Fig.4. and Fig.5. exhibit the simulated spatial and temporal resolutions, which result from the variation of the  $R_s$  of the long-slit streak tube over the range of  $40 \text{ mm} \leq R_s \leq 100 \text{ mm}$  by step of 20 mm. As shown in Fig.4., the spatial resolution for fixed off-axis distance increases to a maximum at  $R_s = 60$  mm and then decreases with increasing  $R_s$ . Decreasing the electron pulses optical path difference plays a dominant role in the spatial resolution improvement. From Fig.4., we can see that the spatial resolution can reach 20 lp/mm at 15 mm off-axis distance while  $R_s = 60$  mm, which means that

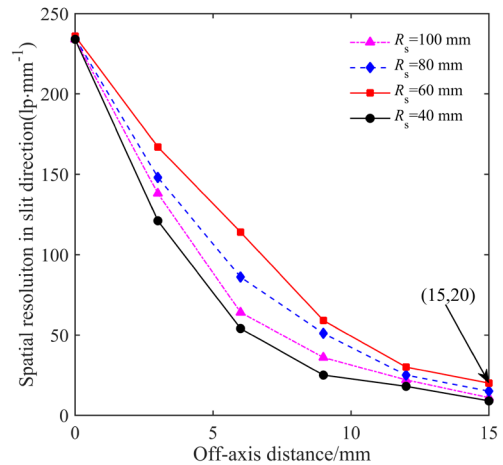


Fig.4. Spatial resolution as a function of  $R_s$  over the range of 40 mm to 100 mm by the step of 20 mm.

the effective photocathode length can reach 30 mm. The temporal resolution is calculated with different  $R_s$  and off-axis distances, as shown in Fig.5. Comparing all these temporal resolutions in fixed off-axis distance, we can see that the temporal resolution almost remains the same value, which indicates that the radius of curvature of the phosphor screen has little effect on the temporal dispersion. Besides, Fig.5. also reveals that there is no much variation at different off-axis distance. It is due to the spherical structure reducing the optical path difference of the photoelectron pulses, which can clearly provide time-resolved consistency.

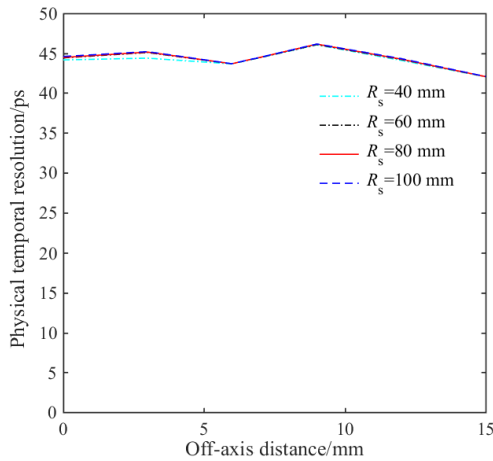


Fig.5. Temporal resolution as a function of  $R_s$  over the range of 40 mm to 100 mm by the step of 20 mm.

#### D. Dependence of the temporal resolution on the $U_{cg}$

Fig.6. exhibits the simulated temporal resolution of this long-slit streak tube, which results from the variation of the accelerating voltage between photocathode and grid over the range of  $50 V \leq U_{cg} \leq 300 V$ . In Fig.6., we observe improving temporal resolution which is a result of increasing  $U_{cg}$ .

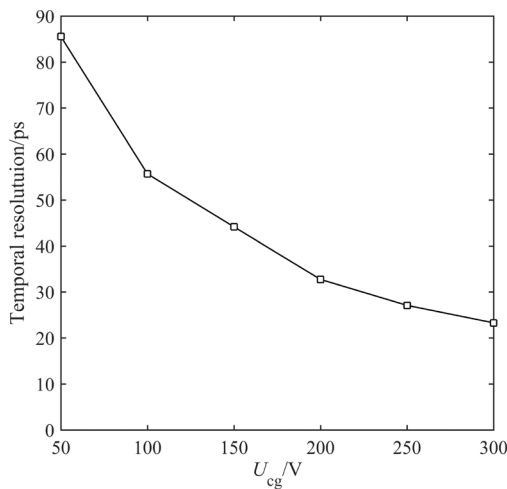


Fig.6. Temporal resolution as a function of  $U_{cg}$  over the range of 50 V to 300 V by step of 50 V.

It is evident, on the one hand, that the electric field intensity between photocathode and accelerating grid increases with increasing  $U_{cg}$ . The stronger electric field could accelerate electrons in a shorter time and improve uniformity of the electron speed to suppress the time dispersion. On the other hand, the stronger electric field gives rise to the shorter electron transit time, which could reduce the space charge effect, thereby helping to decrease the electron longitudinal dispersion to improve temporal resolution. From Fig.6., we can see that the temporal resolution of this long-slit streak tube is better than 90 ps.

#### E. Optimization on the streak tube geometry parameters

Based on the simulation results above, we propose a set of optimized parameters, which are fine-tuned, for better performances. Results in Section 3-B and 3-C show that the higher spatial resolution occurs at  $R_c=85$  mm and  $R_s=60$  mm, which are employed as the optimal value on the radii of curvature (ROCs) of the photocathode phosphor screen. In Section 3-D, we discuss the relationships of temporal resolution to the accelerating voltage,  $U_{cg}$ . We found significant improvement in the temporal resolution with the increasing  $U_{cg}$ . Taking the applied field into account, the long-slit streak tube works in the STIL detection system that acquires the temporal resolution of 50 ps and works stably. Thus, we keep  $U_{cg} = 150$  V. The optimized long-slit streak tube is shown in Fig.7. The spatial and temporal resolution are calculated by using the SMTF and TMTF.

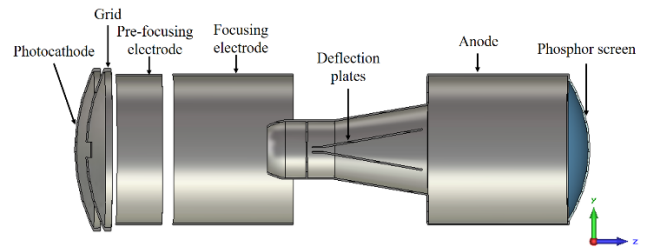


Fig.7. Schematic drawing of the optimized long-slit streak tube.

SMTF at different points on the photocathode (with no regard for spatial resolution limits of the phosphor screen) in slit direction is shown in Fig.8. ( $x$  represents distance from the simulated point to the center of the photocathode). We define the value of the SMTF curve as spatial resolution when it drops to 0.1. From Fig.8., we observe decreasing spatial resolution which is a result of increasing off-axis distance. For one thing, it is because the transit time of electron pulses off-axis from photocathode to phosphor screen is higher than it is on-axis, thereby enlarging the spatial dispersion. For another, the off-axis aberrations of electro-optical system cannot be completely eliminated by using curved spherical photocathode and phosphor screen, which give rise to the larger spatial dispersion, further deteriorating the spatial resolution. Remarkably, the spatial resolution could achieve 22.18 lp/mm at 15 mm off-axis distance, which means that the effective photocathode working length can reach 30 mm if 20 lp/mm is demanded in the STIL system.

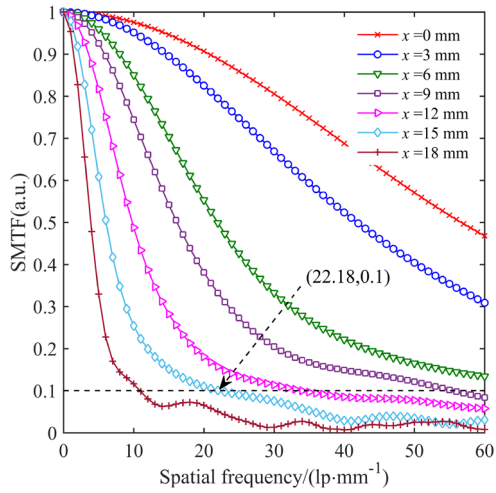


Fig.8. SMTF in slit direction.

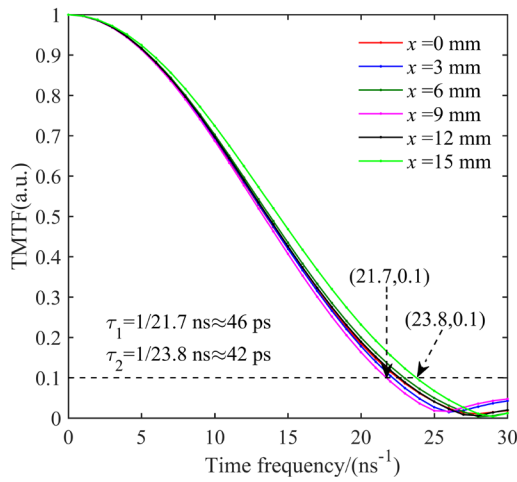


Fig.9. TMTF in different positions on the photocathode.

Fig.9. exhibits the TMTF distributions of the optimized long-slit streak tube in different points on the photocathode for  $U_{cg}=150$  V. Once again, we define the value of the TMTF curve as temporal resolution when it drops to 0.1. It is evident that the temporal resolution varies from 42 ps to 46 ps, which indicates that the curved spherical photocathode and phosphor screen have a better effect on improving the temporal resolution uniformity from the photocathode center to the edge.

4. EXPERIMENT AND DISCUSSION

The manufacture of this optimized long-slit streak tube mainly includes the processing of the photocathode, phosphor screen, and sealed vacuum tube. To make this long-slit streak tube robust for the strong electric-magnetic interference environment and realize detachable sealing structure, it adopts an all-metal-ceramic package. The photocathode adopted a spherical optical fiber as the input window. On the one hand, it can be better coupled with the designed curved spherical photocathode. On the other hand, it can provide a high transmission efficiency. The S-20 photocathode has been utilized for providing a good visible spectral response

from 400 nm to 600 nm.  $Cr_2O_3$  was deposited on the inner surface of the ceramic, which could contribute to avoiding electric breakdown in the vacuum environment. The phosphor screen is a P43 type, since its superiority decay time is often several milliseconds, that can provide a higher frame rate in the STIL system. Fig.10. shows the prototype of this long-slit streak tube.



Fig.10. A prototype of the streak tube.

4.1. Photocathode radiant sensitivity

Photocathode radiant sensitivity (PRS) is measured as the ratio of photocathode current (mA) to the incident radiation power (W) on the photocathode at specified wavelength. In the experiment, a constant DC acceleration voltage of +200 V, which corresponds to a saturated photocurrent, is applied between the photocathode and the grid. In addition, the intensity of the monochromatic light is set to 1 mW/m<sup>2</sup> and the wavelength is of 400 nm to 750 nm. To reduce the influence of non-uniform light and improve the test precision, an optical aperture with  $\Phi 16$  mm is set before the photocathode. The PRS of this long-slit streak tube is graphically represented in Fig.11. The maximum of PRS reaches 61 mA/W at the wavelength of 400 nm.

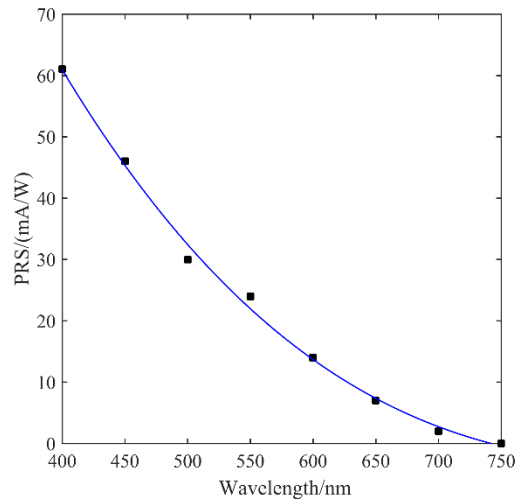


Fig.11. The photocathode radiant sensitivity of the long-slit streak tube.

4.2. Radiant emittance gain

Radiant emittance gain (REG) is measured as the ratio of the total output power (W) on the phosphor screen to the incident monochromatic power (W) on the photocathode at specified wavelength. In the REG test experiment, all high-voltage electrodes, including photocathode, accelerating grid, pre-focusing electrode, focusing electrode, and anode are applied with the working voltage. It should be noted that the deflection plates are located in the anode zero-equipotential zone. The monochromatic light with intensity of  $1 \mu\text{W}/\text{m}^2$  passing through the spectral filters irradiated the photocathode. An optical aperture with  $\Phi 16 \text{ mm}$  was set directly in front of the photocathode to avoid the stray light. Fig.12. exhibits the experimental REG, which results from the variation of the wavelength over the range of  $400 \text{ nm} \leq \lambda \leq 750 \text{ nm}$ . It has almost the same trend as PRS versus wavelength. Besides, the maximum value is 16.9 at the wavelength of 400 nm. Obviously, this long-slit streak tube is of great significance to the visible STIL system.

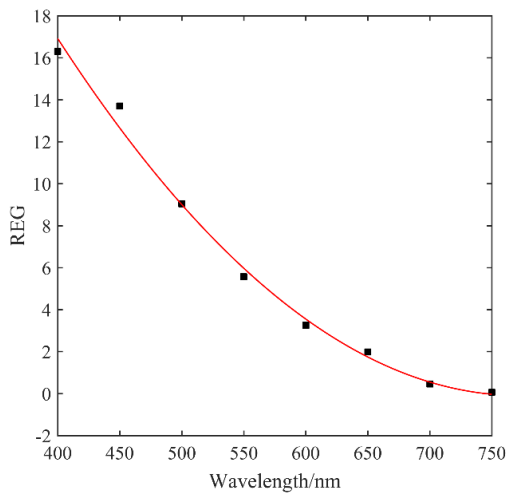


Fig.12. The REG of the long-slit streak tube.

4.3. Spatial resolution

The spatial performance of this long-slit streak tube in static mode is measured by imaging the Three-Linear Target (the

spatial resolution of the Three-Linear Target is shown in Table 2.) without voltage applied on the deflection plates. Additionally, it is defined by the Rayleigh Criterion while the CTF curve results from the obtained image decreased to 0.1. To evaluate the spatial performance over the whole photocathode of this long-slit streak tube, the photocathode is divided into 6 equal parts along the slit direction, shown in Fig.13. In the experiment, the photocathode was directly irradiated with polychromatic 2850K colour temperature source.

Fig.14. shows the target image and we chose the red rectangle area to analyze the CTF. According to the Rayleigh Criterion, the corresponding target can be distinguished completely. From Table 2. and inserted curve, it can be concluded that the spatial resolutions of the streak tube on the photocathode are 16 lp/mm, 18 lp/mm, 20 lp/mm, 20 lp/mm, 18 lp/mm, and 16 lp/mm on the corresponding area, besides, the CTF measurement is 20 %, 16 %, 24 %, 26 %, 16 %, 16 %, respectively. Furthermore, the areas a) and f) are about 15 mm away from the photocathode center. Thus, the spatial resolution of this long-slit streak tube can reach 16 lp/mm over the entire 30 mm-length photocathode area. The measurements are lower than the simulations, mainly due to the limitation of e thphosphor screen, assembly and coupling error of the streak tube.

Table 2. Spatial resolution of the Three-Linear Target.

Target Model	4-1	4-2	4-3	4-4	4-5	4-6
Spatial resolution/(lp/mm)	16	18	20	23	25	28

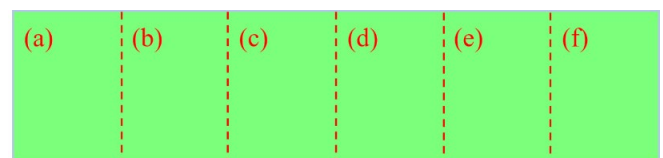


Fig.13. The division position distributions of 6 different areas on the photocathode.

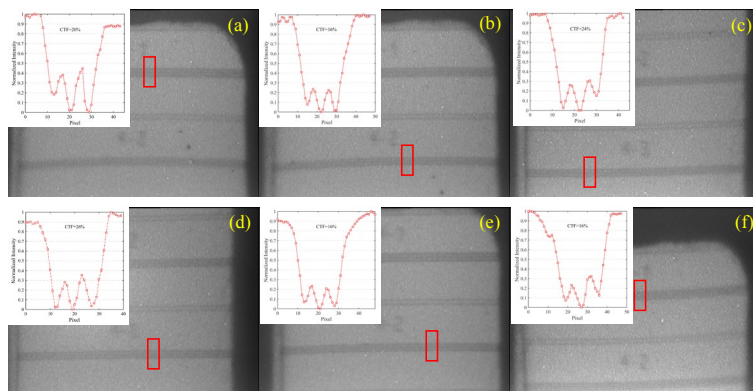


Fig.14. Spatial resolution under the Linear Target. a) At off-axis -15 mm: 16 lp/mm; b) At off-axis -10 mm: 18 lp/mm; c) At off-axis -5 mm: 20 lp/mm; d) At off-axis 5 mm: 20 lp/mm; e) At off-axis 10 mm: 18 lp/mm; f) At off-axis distance 15 mm: 16 lp/mm.

## 5. CONCLUSIONS

Computer models are developed to investigate the spatio-temporal performances of the long-slit streak tube for a better operating and geometry conditions based on the M-C method and MTF (SMTF and TMTF). Simulations illustrate that spatial resolution varies significantly at different  $R_c$ . In the range of 75 mm to 95 mm, there exists an optimum  $R_c$  corresponding to the maximum spatial resolution. Similarly, the curvature radius of the phosphor screen plays a great role in the spatial resolution improvement. Moreover, the temporal resolution is a function of  $U_{cg}$ . With the increasing  $U_{cg}$ , the temporal resolution improves. A set of long-slit streak tube geometry parameters of  $R_c=85$  mm,  $R_s=60$  mm are proposed for the streak tube structural optimization. Theoretical results show that the optimized spatial resolution is higher than 22 lp/mm over the whole 30 mm-length photocathode, and the temporal resolution calculated is better than 50 ps at  $U_{cg}=150$  V. Long-slit streak tube manufactured according to the optimization can experimentally achieve a spatial resolution of higher than 16 lp/mm and a large-format photocathode of 30 mm-length. The tested PRS and REG show that this streak tube has good imaging performance in the visible spectrum. Following the improvement of the spatial resolution, there is a significant expansion of the application detection accuracy and fields of the streak tube.

## ACKNOWLEDGMENT

This study was supported by the Scientific Instrument Developing Project of the Chinese Academy of Sciences (Grant No. GJJSTD20190004), the Open Research Fund of State Key Laboratory of Transient Optics and Photonics (Grant No. SKLST202012), the Ph.D. Project supported by the Jinling Institute of Technology (No. jit-b-202012), and Youth Innovation Promotion Association CAS (Grant No. 2021402).

## REFERENCES

- [1] Howorth, J.R., Milnes, J.S., Fisher, Y., Jadwin, A., Boni, R., Jaanimagi, P.A. (2016). The development of an improved streak tube for fusion diagnostics. *Review of Scientific Instruments*, 87 (11), 287-294.
- [2] Xia, W., Han, S., Ullah, N., Cao, J., Wang, L., Cao, J., Cheng, Y., Yu, H. (2017). Design and modeling of three-dimensional laser imaging system based on streak tube. *Applied Optics*, 56 (3), 487-497.
- [3] Ye, G., Fan, R., Lu, W., Dong, Z., Li, X., He, P., Chen, D. (2016). Depth resolution improvement of streak tube imaging lidar using optimal signal width. *Optical Engineering*, 55 (10), 103112.
- [4] Ageeva, N.V., Andreev, S.V., Belolipetski, V.S., et al. (2009). Small-size meshless 50 ps streak tube. In *28<sup>th</sup> International Congress on High-speed Imaging and Photonics*. SPIE, 71260A.
- [5] Lerche, R.A., Andrews, D.S., Bell, P.M., Griffiths, R.L., Huey, A.W., McDonald, J.W., de Dios, V.G. (2004). *Comparison of streak tube performance*. UCRL-TR-208078, Lawrence Livermore National Laboratory, Livermore, CA (US).
- [6] Feldman, G.G., Jilkina, V.M., Razdobarin, G.T. (1998). PV-400 picosecond streaktube with large format photocathode. *Optical Engineering*, 37 (8), 2247-2248.
- [7] Tian, L., Shen, L., Chen, L., Li, L., Tian, J., Chen, P., Zhao, W. (2021). A new design of large-format streak tube with single-lens focusing system. *Measurement Science Review*, 21 (6), 191-196.
- [8] Hui, D., Luo, D., Tian, L., et al. (2018). A compact large-format streak tube for imaging lidar. *Review of Scientific Instrument*, 89 (4), 045113.
- [9] Feng, J., Shin, H.J., Nasiatka, J.R., Wan, W., Young, A.T., Huang, G., Comin, A., Byrd, J., Padmore, H.A. (2007). An xray streak camera with high spatio-temporal resolution. *Applied Physics Letters*, 91 (13), 134102.
- [10] Tian, L.P., Li, L.L., Wen, W.L., Wang, X., Chen, P., Lu, Y., Wang, J.F., Zhao, W., Tian, J.S. (2018). Numerical calculation and experimental study on the small-size streak tube. *Acta Physica Sinica*, 67 (18), 188501.
- [11] Tian, J.S. (2020). Introduction to development of streak and framing cameras. *High Power Laser and Particle Beams*, 32 (11), 112003.
- [12] Liu, X.L., Tian, J.S., Tian, L.P., et al. (2021). A synchroscan streak tube with high deflection sensitivity. *Acta Physica Sinica*, 70 (21), 218502.
- [13] Tian, L., Shen, L., Li, L., Wang, X., Chen, P., Wang, J., Chen, L., Zhao, W., Tian, J. (2021). Small-size streak tube with high edge spatial resolution. *Optik*, 242, 166791.

Received November 14, 2021  
Accepted January 28, 2022